ISIJ International, Vol. 43 (2003), No. 12, pp. 2038–2045

Production and Properties of Nano-scale Oxide Dispersion Strengthened (ODS) 9Cr Martensitic Steel Claddings

Shigeharu UKAI, Takeji KAITO, Satoshi OHTSUKA, Tsuyoshi NARITA, Masayuki FUJIWARA[1)] and Toshimi KOBAYASHI[2)]

O-arai Engineering Center, Japan Nuclear Cycle Development Institute, Narita, O-arai, Ibaraki 311-1393 Japan.
1) Kobelco Research Inc., Kobe, Hyogo 651-2271 Japan. 2) Sumitomo Metal Technology, Ltd., Amagasaki, Hyogo 660-0856 Japan.

(*Received on August 23, 2003; accepted in final form on June 26, 2003*)

The 9Cr–ODS martensitic steel claddings were developed by cold-rolling and subsequent heat-treatment. The standard chemical composition is Fe–0.13C–9Cr–2W–0.2Ti–0.35Y_2O_3. The substantially elongated grains formed by cold-rolling turned out to be into equi-axied grains by ferrite to austenite phase transformation at the final heat-treatment. The produced claddings have the tempered martensitic structure and excess oxygen of 0.060 mass%. The superior tensile and creep rupture strength were shown in the produced cladding, compared with conventional ferritic (PNC–FMS) and even austenitic (PNC316) claddings at higher temperature and extended time. The strength improvement is attributed to finely distributed nano-scale complex oxide. The coarser ferrite grains produced by slow cooling make further improvement in the tensile and creep rupture strength beyond those of tempered martensite at high temperature and longer testing time. The higher excess oxygen content of 0.137 mass% prevents fine distribution of the oxide particles that lead to inferior high temperature tensile and creep strength.

KEY WORDS: ODS; yttria; phase transformation; martensite; ferrite; excess oxygen; cladding; tensile strength; creep rupture strength; cold rolling; grain size.

1. Introduction

To improve thermal efficiency of plants operating at high temperature, efforts have being made to develop high temperature strength of ferritic–martensitic steels (FMS). The effects of alloying elements and heat-treatment to stabilize carbide precipitates have been studied in the field of the power-generation industry.[1)] The oxide dispersion strengthened (ODS) martensitic steel is expected to be a good candidate of the materials having a potential of superior high temperatures strength over 923 K. Since FMS is well known to have far superior radiation resistance compared with austenitic steels, the ODS martensitic steel is expected to be a promising cladding material in the long-life core of fast reactor fuel pins[2–6)] as well as a low activated fusion reactor materials.[7)] The development of ODS martensitic steel has being conducted in Japan Nuclear Cycle Development Institute (JNC). The chemical composition of the material for fuel cladding application to fast reactors was proposed to be Fe–0.13C–9Cr–2W–0.2Ti–0.35Y_2O_3, and substantially elongated grains formed by cold-rolling were made into equi-axied grains by means of α to γ phase transformation.[8,9)]

In this study, claddings with a standard composition of Fe–0.13C–9Cr–2W–0.2Ti–0.35Y_2O_3 are developed using the cold-rolling process, and the high temperature mechanical properties of the produced claddings are investigated. The effects of difference of the final heat-treatment and oxygen content on the mechanical properties of the 9Cr–ODS martensitic steels are extensively studied.

2. Experimental Procedure

2.1. Cladding Production and Heat Treatment

The preparation process of the ODS martensitic claddings is shown in **Fig. 1**. As the raw material powders, two kinds of powders: the Fe–0.13C–9Cr–2W–0.2Ti powders atomized in argon gas with a particle size below 150 μm and mixture of each element powder (Fe, C, Cr, W, Ti) measured in the same nominal composition were used for making M11/MS11 claddings and Mm13 claddings, respectively. Mechanically alloying of raw material powders with Y_2O_3 powders of 20 nm mean diameter was performed using an attrition type ball mill rotating at a speed of 220 rpm for 48 h in argon gas atmosphere with 10 kg batches. In this experiment, two milling conditions were employed; one for M11 and MS11 claddings and another for Mm13 claddings. From experimental restraint on an attrition type ball mill, the agitator rod for Mm13 was 210 mm long and that for M11 and MS11 was 200 mm long. The milling energy is slightly higher in Mm13 than M11 and MS11. The milled powders were then sealed in 67 mm diameter cans, and degassed at 673 K in 0.1 Pa vacuum for 2 h. Raw bars of 25 mm diameter were produced by hot-extrusion at an

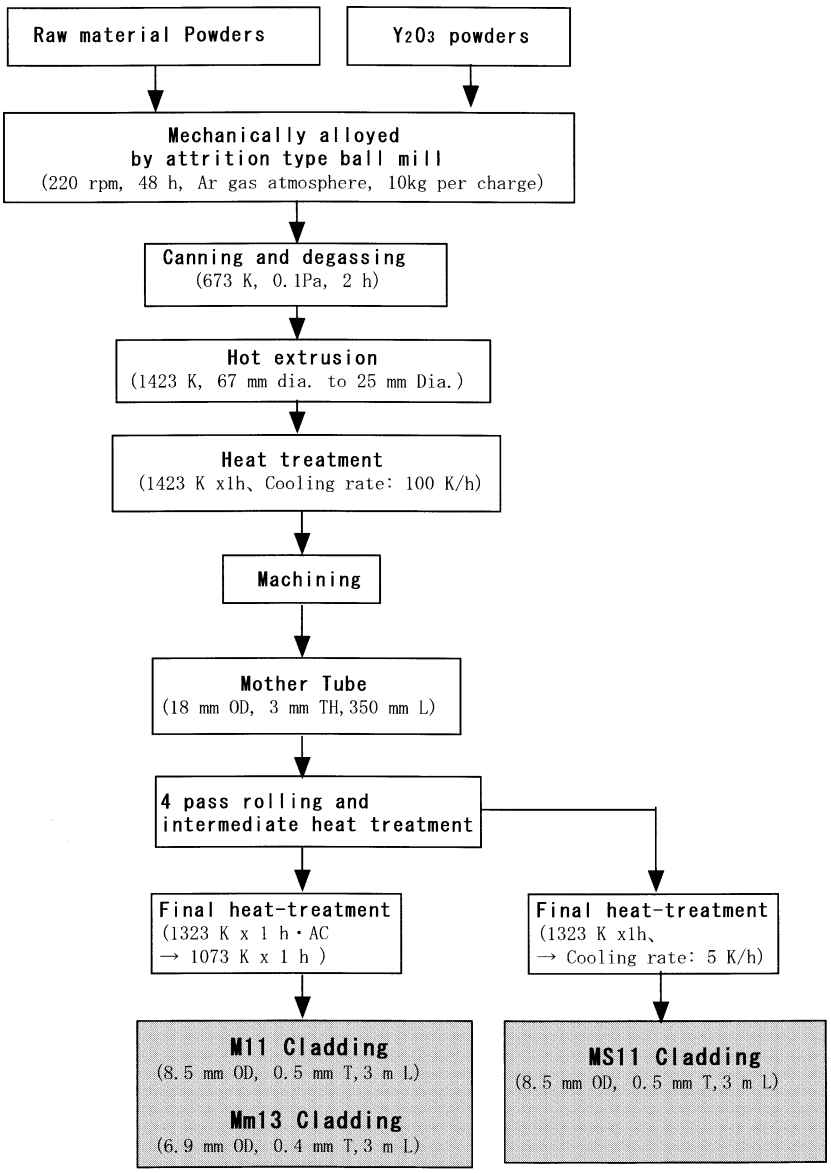

Fig. 1. Flow of process followed in production of M11, MS11 and Mm13 claddings.

1 423 K.

The raw bars were machined and drilled to form the mother tubes with 18 mm outer diameter, 3 mm wall-thickness and 350 mm length. M11 and MS11 claddings in the dimension of 8.5 mm outer diameter, 0.5 mm thickness and near 3 m length were produced by four-pass cold rolling using pilger mill. While, the Mm13 cladding was produced into the dimension of 6.9 mm outer diameter, 0.4 mm thickness and near 3 m length by the same process of four-pass cold rolling. The cold-rolling of these claddings was conducted at a state of the ferritic structure obtained by low cooling rate of 150 K/h in the furnace after normalizing at 1 323 K. **Figure 2** represents the results of hardness change in the course of cold-rolling process of M11 cladding. A reduction (Rd) of the cold-rolling attains around 45% at each pass. The employed normalizing (1 323 K for 30 min) and furnace cooling (cooling rate of 150 K/h) after each cold-rolling successfully softened the claddings.

After final cold-rolling, normalizing at 1 323 K for 1 h in vacuum and subsequent cooling in argon gas atmosphere at cooling rate of 5 000 K/h and tempering at 1 073 K for 1 h were applied for M11 and Mm13 claddings. These heat treatments were applied to change elongated grain structure generated in the cold-rolling process to equi-axied one, by means of α to γ and γ to martensite phase transformations. On the other hand, MS11 cladding was normalized at 1 323 K for 1h followed by the furnace cooling at cooling rate of 5 K/h to make the ferrite phase at the final stage.

2.2. Test of Mechanical Properties and Microstructural Observation

The produced claddings are tested to determine their high temperature mechanical properties by means of ring tensile[10] and internally pressurized creep rupture tests. These tests were selected to prove their resistance against the dominant direction of loading in an actual fuel pin, *i.e.* hoop direction. In order to characterize the mechanical properties of the manufactured claddings, the optical micrographs were taken. The transmission electron microscopy (TEM) observations of the thin foil were made using a Hitachi H-800 to determine the dispersion parameters, especially the size and number density of oxide parti-

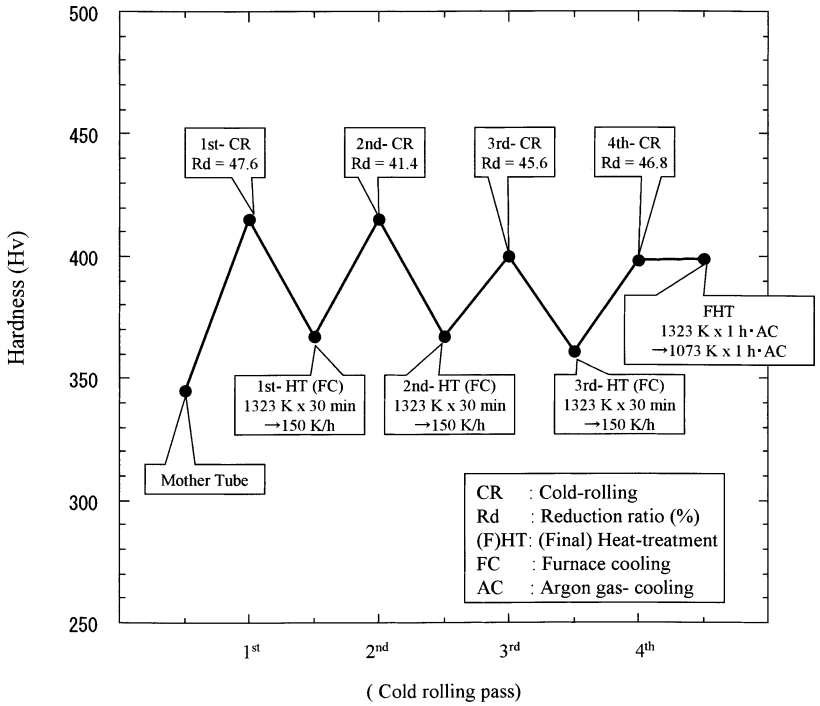

Fig. 2. Hardness change in the course f M11 cladding produced by means of cold-pilger mill rolling and subsequent intermediate heat-treatment.

Table 1. Chemical composition on produced claddings (mass%).

Cladding	Chemical composition (mass%)									
	C	Cr	W	Ni	Ti	Y	N	Ar	Y_2O_3*1	Ex.O*2
M11, MS11	0.13	9.00	1.95	0.021	0.20	0.29	0.013	0.0025	0.37	0.060
Mm13	0.14	8.85	1.95	0.010	0.20	0.27	0.010	0.0054	0.34	0.137

Si : 0.05 (M11, MS11), <0.005(Mm13)
Mn : 0.04 (M11, MS11), <0.01(Mm13)
P : 0.002(M11, MS11), 0.001(Mm13)
S : 0.002(M11, MS11), 0.003(Mm13)

*1 : Estimated from yttrium content assuming it to be contained in the form of Y_2O_3 (yttrium mass % x 1.27)
*2 : Excessive oxygen estimated as total oxygen content minus oxygen content in Y_2O_3 (total oxygen content – ytrium mass % x 0.27)

cles. The electron diffraction and EDX analyses for precipitates in the extracted replicas were conducted to characterize the carbide and oxide precipitates.

3. Result

3.1. Chemical Composition and Microstructure

The measured chemical composition of the manufactured claddings are listed in **Table 1**. The target chemical composition is Fe–0.13C–9Cr–2W–0.2Ti–0.35Y_2O_3, where the amount of 2.0 mass% W for solution hardening and 0.20 mass% Ti were added. The value of excess oxygen (Ex.O) was estimated by subtracting oxygen contained in Y_2O_3 from the total oxygen determined by inert gas melt method. The Y content was analyzed by the inductively coupled plasma method, from which the Ex.O and Y_2O_3 contents were estimated. The Mm13 cladding has higher content of excess oxygen of 0.137 mass% compared with M11 and MS11 claddings. This could be due to the introduction of higher energy and use of elemental powders during mechanically alloying.

The optical micrographs of M11, Mm13 and MS11 claddings are shown in **Fig. 3**. The tempered martensitic structure is formed in the whole area of M11 and Mm13 claddings. The finely elongated phases of about 30 to 100 μm in length are also observed in strips by the white color in M11 cladding. The white color is considered not to be δ-ferrite, but could be non-transformed α phase remained without transformation during normalizing and cooling, since this material was produced by mechanically alloying at room temperature without melting. In M11 cladding with 0.060 Ex.O, it is supposed that the carbon content in the matrix is likely reduced due to Ti–C formation rather than Ti–O formation. On the other hand, in Mm13 cladding with

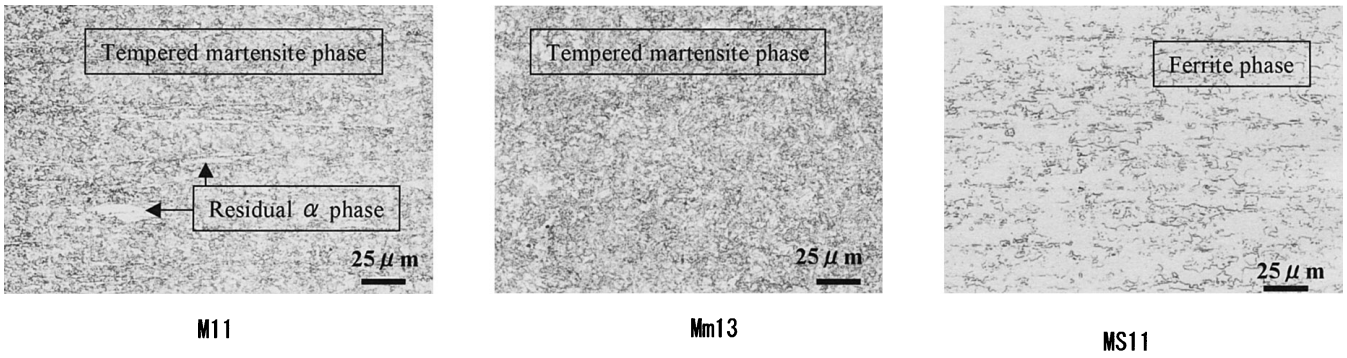

Fig. 3. Optical micrographs of M11, Mm13 and MS11 claddings.

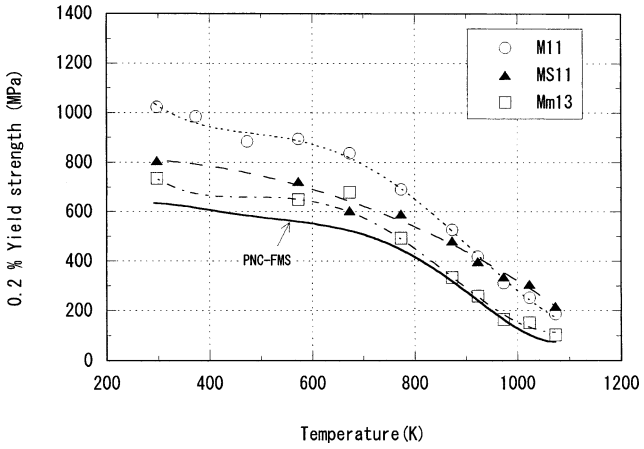

Fig. 4. 0.2% yield strength in the hoop direction using the ring specimens of M11, MS11 and Mm13 claddings at different temperature, comparing with conventionl PNC–FMS.

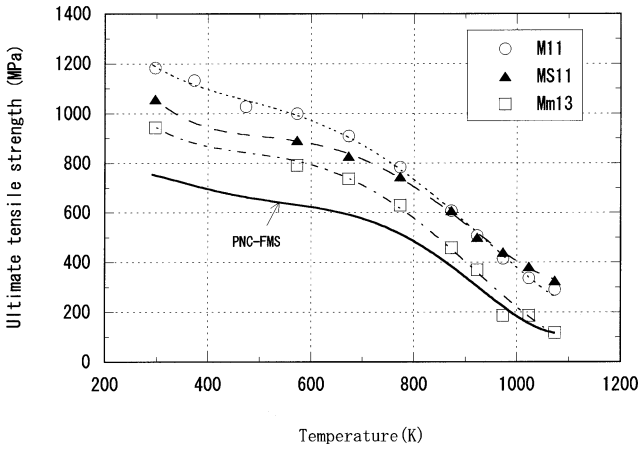

Fig. 5. Ultimate tensile strength in the hoop direction using the ring specimens, together with PNC–FMS.

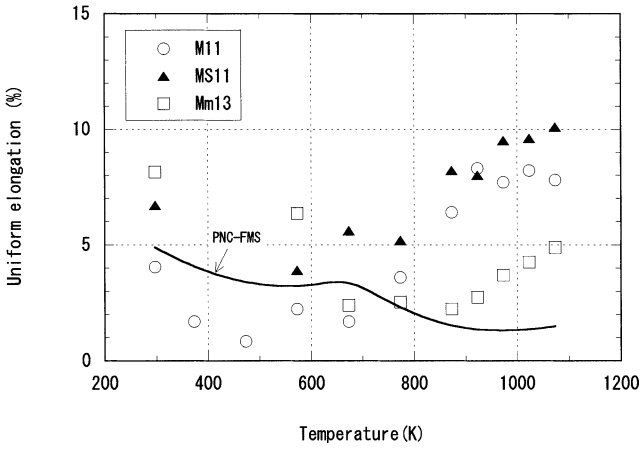

Fig. 6. Uniform elongation in the hoop direction using the ring specimens of M11, MS11 and Mm13 claddings, comparing with PNC–FMS.

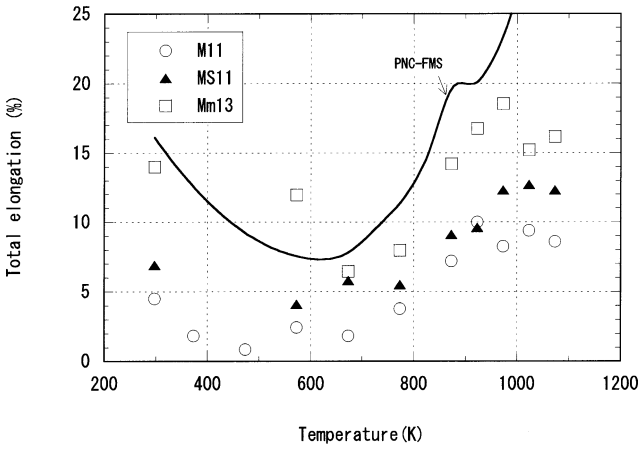

Fig. 7. Total elongation in the hoop direction using the ring specimens of M11, MS11 and Mm13 claddings, comparing with PNC–FMS.

0.137 Ex.O, C content could be maintained, and α to γ phase transformation is perfectly taken place. The MS11 cladding has the coarser ferrite grains with about 20 μm, which were formed by γ to α phase transformation and grain growth occurred concomitantly during furnace cooling at cooling rate of 5 K/h after normalizing at 1 323 K for 1 h.

3.2. Tensile Properties

The 0.2% yield strength and ultimate tensile strength of M11, MS11 and Mm13 claddings in the hoop direction measured in the temperature range from room temperature to 1 073 K are shown in **Figs. 4** and **5**, together with the corresponding data of ferritic–martensitic stainless steel (PNC–FMS) used conventionally as fast reactor fuel cladding.[11] All the three claddings present superior strength compared with conventional PNC–FMS. Among the claddings, the Mm13 showed the lowest strength, and this reason will be discussed later. Comparing M11 and MS11, the strength of MS11 is higher at above 900 K. This is probably due to the coarser ferritic grains in MS11 formed by low cooling rate (5 K/h) from the austenite.

The uniform and total elongations from room temperature to 1 073 K are shown in **Figs. 6** and **7**, together with

those of conventional PNC–FMS. In the temperature range from 673 to 973 K, where the fast reactor is commonly operated, the measured uniform elongation satisfies the value of 0.3 % required for design. Particularly, all the produced claddings present superior uniform elongation to PNC–FMS at above 800 K, although their total elongations are smaller than PNC–FMS over the entire temperature range. This advantage of superior elongation in the produced claddings is probably ascribed to the pining of dislocations by Y_2O_3 particles, which retard recovery and sustain work-hardening. Smaller total elongation of the produced claddings could be caused by the limited amount of necking after uniform elongation.

3.3. Creep Rupture Properties

The measured data on creep rupture strength in hoop direction under internal pressure (hoop stress) at 973 K are indicated in **Fig. 8**. Mm13 exhibits significantly low creep rupture strength, similar to the strength level of PNC–FMS. The M11 and MS11 have almost same creep rupture strength, where the regression line for M11 is the result of analysis using the creep rupture data at temperature of 923 K, 973 K and 1 023 K, that is expressed in detail in the next session. The rupture time for MS11 seems to extend to the longer time, because MS11 specimen did not rupture up to 10 784 h at 130 MPa, as indicated by arrow mark.

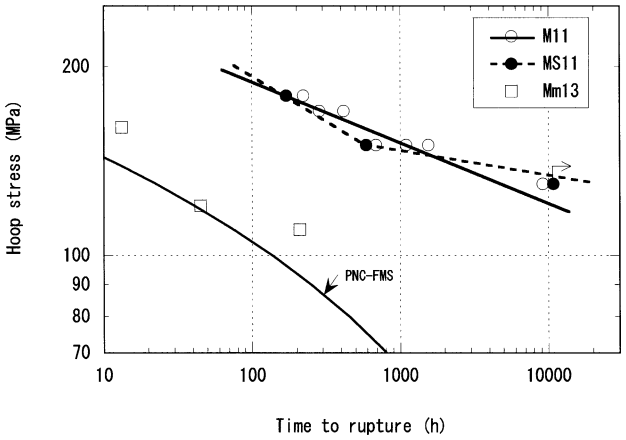

Fig. 8. Internal creep rupture curve of M11, MS11 and Mm13 claddings at 973 K, comparing with conventional PNC–FMS.

4. Discussion

4.1. Internal Creep Rupture Properties of M11 Cladding

The internal creep rupture data of M11 cladding were acquired at 923 K, 973 K and 1 023 K, and were analyzed applying Larson–Miller-Parameter (LMP) that is expressed in terms of temperature and rupture time. The regression analysis of the least square method was conducted for the hoop stress *vs*. LMP to minimize the standard deviation. The best-fit curve with the optimized values is represented in **Fig. 9**. The largest value of LMP tested is 22 180 at 1 023 K, where the cladding has not yet ruptured, as indicated by the arrow mark in Fig. 9. The value of LMP=22 180 is converted to the equivalent rupture time at the typically operational temperature of 973 K in fast reactor as 106 900 h at 973 K. This period is adequately longer than 5 years service of fuel elements.

The lifetime of the fast reactor fuel pin is dominated by the internal creep rupture strength of the cladding induced by the fission gas internal pressure at temperature around 973 K. In **Fig. 10**, internal creep rupture data are shown at 923 K, 973 K and 1 023 K for M11 cladding. The best-fit curves for hoop stress *vs*. rupture time derived above are also shown by solid curves at each temperature. The corresponding creep rupture curves for PNC–FMS and austenitic PNC316 are also presented for comparison in this figure. PNC316 is the typical austenitic cladding developed by JNC in the fast reactor program.[12] Notably superior performance in rupture time is shown in M11 cladding compared

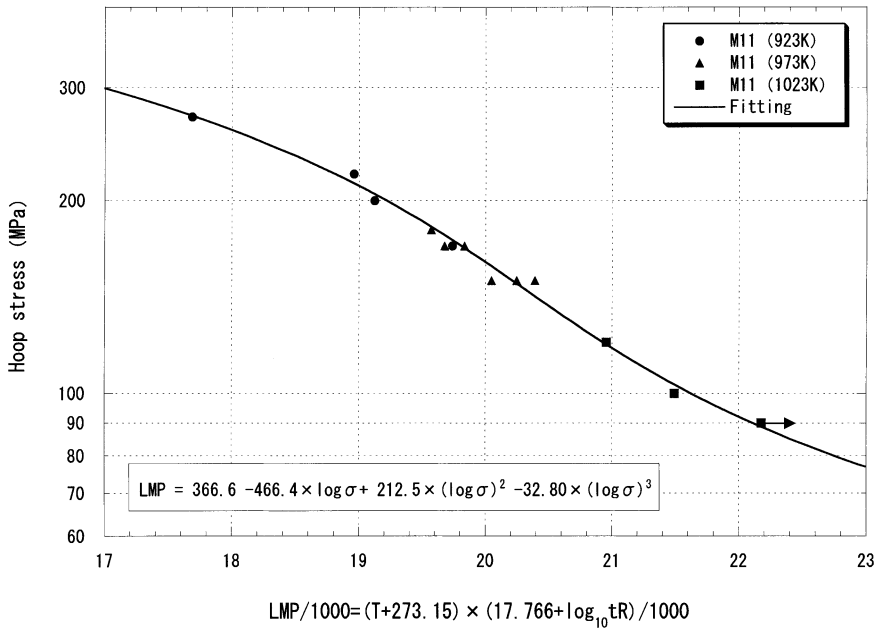

Fig. 9. Best-fit curve of M11 rupture strength at 923 K, 973 K and 1 023 K drawn by regression analysis against Larson–Miller parameter.

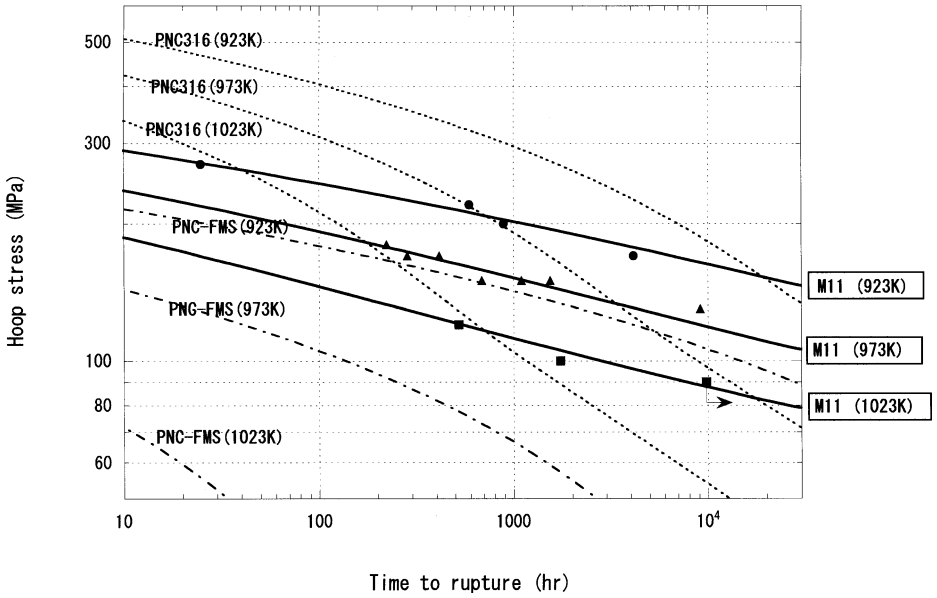

Fig. 10. Internal creep rupture curve of M11, MS11 and Mm13 claddings at 923 K, 973 K and 1 023 K, comparing with ferritic PNC–FMS and austenitic PNC316.

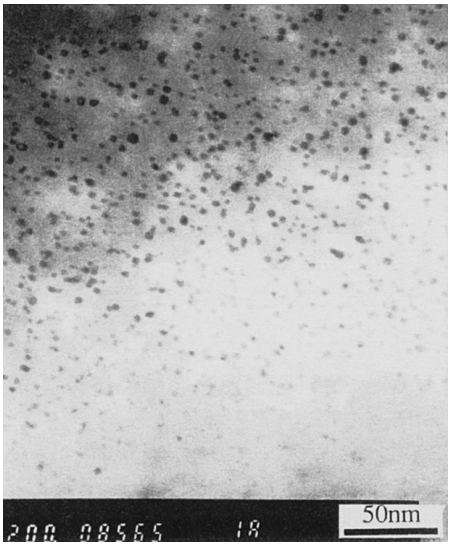

Fig. 11. Typical high-magnification on transmission electron micrographs of oxide particles in M11 cladding.

with PNC–FMS. The slop of PNC316 is steeper than M11, crossing over that it before 1 000 h at 1 023 K and before 10 000 h at 973 K. The stress condition of the fast reactor fuel pin gradually increases due to accumulation of fission gases up to around 100 MPa during service duration of 44 000 h at 973 K. Therefore, it is to be noted that M11 cladding is of advantage compared with austenitic PNC316 cladding under the real fast reactor operation condition.

Figure 11 is a transmission electron micrograph of M11, showing nearly spherical shape of Y_2O_3 particles in the martensite matrix. The oxide particle size is around 3 nm, and inter-particles spacing is significantly shortened. Considering that high temperature strength of ODS steels is owing to an existence of oxide particles that act as a resistance for dislocation gliding,[13] the creep rupture strength measured in M11 is dominated by those oxide particles distributed finely. The creep rupture strength of austenitic PNC316 is attributed to the formation of Ti–Nb carbide precipitates. Those precipitates have a tendency to become coarser, and thus creep rupture strength concomitantly falls at longer time and at higher temperature.[14] On the other hand, Y_2O_3 particles are thermally stable at the extended duration, which is owing to the sustainable creep rupture strength of M11 even at temperature over 973 K and longer time.

4.2. Effect of Final Heat-treatment on the High Temperature Strength (M11 *vs.* MS11)

When compared MS11 with M11 using the data shown in Figs. 4 to 7, MS11 cladding exhibited superior tensile strength at above 873 K and adequate ductility over entire temperature range. The creep rupture strength also showed the extended lifetime in MS11 cladding at 973 K. These results indicate that high temperature mechanical properties of 9Cr–ODS martensitic steel cladding are improved by morphological change induced by the final heat-treatment.

The continuous cooling transformation (CCT) diagram[9] of M11 cladding in the cooling rates ranging from 50 to 18 000 K/h is shown in **Fig. 12**. In this diagram, martensite start (Ms) and finish (Mf) lines and ferrite start (Fs) and finish (Ff) lines are shown. M11 and Mm13 was cooled at rate of approximately 5 000 K/h from austenite and tempered at 1 073 K for 1 h. Thus M11 and Mm13 claddings have tempered martensite, as shown in Fig. 3. On the other hand, the microstructure of MS11 cladding is coarse ferrite grains of around 10 μm size and carbide, since its cooling rate is 5 K/h that intersect with only Fs and Ff lines, as shown in Fig. 12.

Since Y_2O_3 particles distribution in M11 and MS11 is almost same, the superior strength of MS11 cladding at high temperature could be attributed to the grain structure: a coarser ferrite grain in MS11 *vs*. extremely fine martensite grains of less than 1 μm size in M11. In the previous study,[9] the existence of grain-boundary sliding was pointed out for the creep deformation of the martensitic 9Cr–ODS cladding with extremely fine and homogeneous grains at 973 K. Therefore, it is considered that the suppressed grain-

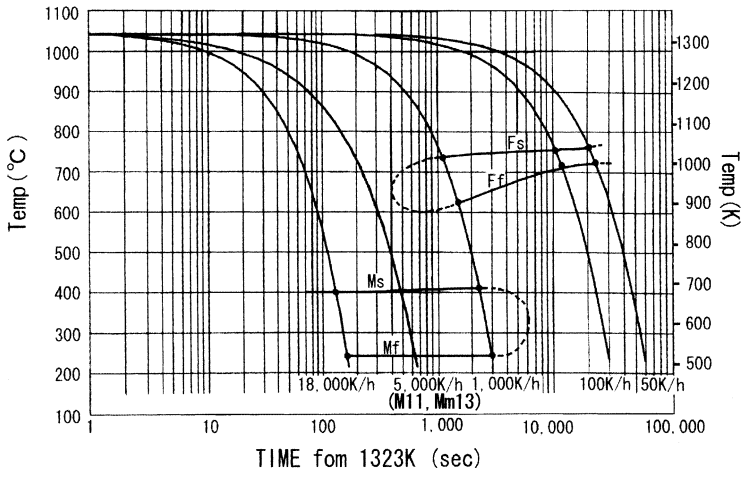

Fig. 12. Continuous cooling transformation (CCT) diagram of M11 cladding.

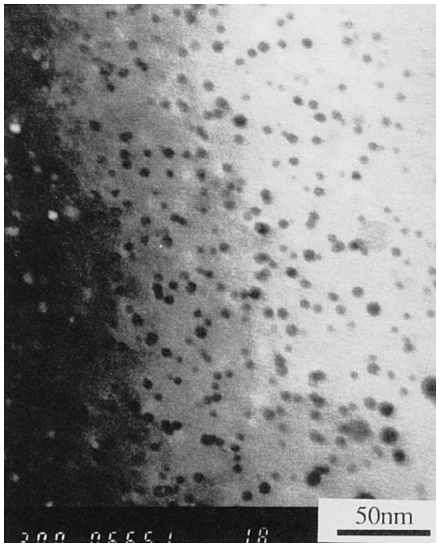

Fig. 13. Transmission electron micrograph of oxide particles in Mm13 cladding.

boundary sliding contribution due to coarser grains in MS11 cladding is attributed to the superior tensile and creep rupture strength at higher temperature and longer time.

4.3. Effect of Excess Oxygen on the High Temperature Strength (M11 *vs.* Mm13)

Mm13 exhibited the inferior tensile and creep rupture strength compared with M11. The transmission electron mircrograph of the oxide particles in Mm13 specimen is shown in **Fig. 13**. The size of the observed oxide particles is more than 5 nm, which is slightly coarser than that of M11 specimen shown in Fig. 11. In particular, the number density of the oxide particles is low in Mm13, and relatively longer inter-particles spacing in Mm13 than M11 leads to the lower strength in Mm13 from the inverse relation of a strength level to the inter-particles spacing.[13)]

The co-authors found out by means of X-ray diffraction analysis that Y_2O_3 particles are dissolved in the matrix during mechanically alloying process, and then fine complex oxide with Y and Ti precipitates during the hot-extrusion process at 1 423 K.[15)] Hence, the size of precipitates which appear during the hot-extrusion at 1 423 K would depend on the amount of Y, Ti and excess oxygen contents in the matrix. Among these elements, major difference between M11 and Mm13 is excess oxygen content as shown in Table 1. Therefore, the effect of the excess oxygen on the size of precipitates is investigated by means of TEM observation and thermodynamic analysis, focusing on partition of titanium element between Y_2O_3 particles and others.

TEM observation of extracted replicas was carried out for the precipitates of M11 and Mm13 normalized at 1 323 K, and results are summarized in **Table 2**. In M11 with lower excess oxygen of 0.06 mass%, three types of precipitates are identified: $M_{23}C_6$ containing Ti (several hundred nm), Ti oxide (Ti–O) (a hundred nm) and Y–Ti oxide (3 nm size). The $M_{23}C_6$ was identified from the lattice constant measured by electron diffraction analysis. Ti oxide and Y–Ti oxide were estimated from the EDX analysis of each particle. Their chemical composition can not be exactly distinguished by electron diffraction analysis. In Mm13 specimen with higher excess oxygen of 0.137 mass%, however, several hundred nm size of Cr_2O_3 containing titanium was identified, together with a hundred nm size of $YCrO_3$ oxide containing titanium and finely distributed Y–Ti oxide particles in more than 5 nm size. The Cr_2O_3 and $YCrO_3$ were identified from the electron diffraction analysis. The carbide containing titanium was not be observed.

The effect of excess oxygen on the oxide formation is thermodynamically investigated. Using Thermo-Calc code,[16)] equilibrium phases are calculated at 1 423 K that corresponds to the oxide precipitation temperature during hot-extrusion. In the lack of thermodynamic data of Y–Ti complex oxide, however, complex oxide formation can not be taken into account; Y_2O_3 and Ti oxide are separately calculated in this calculation. The titanium partitioning between oxide and carbide is paid attention in this calculation. In the case of M11 with lower excess oxygen content, Ti exists in three phases as shown in Table 2: 0.05 mass% in TiC, 0.10 mass% in Ti_2O_3, and 0.05 mass% in matrix γ phase. On the other hand, in Mm13 containing higher excess oxygen content, all of Ti precipitate as Ti_4O_7. With increasing excess oxygen content from 0.06 mass% (M11) to 0.137 mass% (Mm13), the higher order of titanium oxide, Ti_4O_7, instead of Ti_2O_3 is predicted. Furthermore, chromi-

Table 2. Results of TEM and Thermo-calc analyses on precipitates.

Cladding	TEM analysis (as-normalized at 1323 K)	Thermo-Calc analysis at 1423K
M11 (Ex.O=0.060mass%)	・$M_{23}C_6$ containing titanium (several hundred nm size) ・Titanium oxide (Ti-O) (a hundred nm size) ・Y-Ti oxide (3 nm size) ・Martensite and Non-transformed Ferrite	γ + TiC + Ti_2O_3 + Y_2O_3 Ti in TiC : 0.05 mass % Ti in Ti_2O_3 : 0.10 mass % Ti in γ phase matrix : 0.05 mass % Y_2O_3 : 0.34 mass % C in γ Phase matrix : 0.118 mass %
Mm13 (Ex.O=0.137mass%)	・Cr_2O_3 containing titanium (several hundred nm size) ・$YCrO_3$ containing titanium (a hundred nm size) ・Y-Ti oxide (larger than 5 nm size) ・Martensite	γ + Ti_4O_7 + Cr_2O_3 + Y_2O_3 Ti in Ti_4O_7 : 0.20 mass % Y_2O_3 : 0.34 mass % Cr_2O_3 : 0.077 mass % C in γ Phase matrix : 0.130 mass %

um oxide as a type of Cr_2O_3 is predicted for the higher excessive oxygen specimen of Mm13. These thermodynamic predictions well coincide with the results of TEM observation. The improved tensile and creep rupture strength in M11 cladding compared with that of Mm13 cladding is owing to the formation of finer nano-meter size Y–Ti complex oxide. This finer complex oxide formation could be associated with the formation of lower order of titanium oxide, Ti_2O_3, with lower excess oxygen. It is supposed that nano-meter size Y–Ti complex oxide would be formed by the precipitation as Y_2O_3–Ti_2O_3 during hot-extrusion process under lower excess oxygen content.

5. Conclusion

In this study, 9Cr–ODS steel claddings were originally developed and produced by cold-rolling in ferrite condition with parameters of final heat-treatment and excess oxygen content. The results of study are summarized as follows.

(1) The produced claddings in tempered martensitic structure (M11) attained the noticeable improvement in tensile and internal creep rupture strength due to fine distribution of the oxide particles in martensite matrix.

(2) A coarser ferrite grains of about 20 μm size were produced by slow cooling rate of 5 K/s in 9Cr–ODS steel (MS11). Those coarser ferritic grains promoted to the further improvement beyond that of tempered martensitic steels in the tensile and creep rupture strength at high temperature and longer time.

(3) The excess oxygen has significant influence on the high temperature mechanical properties; higher excess oxygen content (Mm13) prevents formation of finely distributed oxide particles, which induces inferior high temperature tensile and creep strength.

REFERENCES

1) Proc. Conf. Advanced Heat Resistant Steels for Power Generation, ed. by R. Viswanathan and J. Nutting, IOM Communication Ltd., London, (1999).
2) J. J. Huet: *Nucl.Technol.*, **70**, (1985), 215.
3) A. Alamo, H. Regle, G. Pons and J. L. Bechade: *Mater. Sci. Forum*, **88–90**, (1992), 183.
4) P. Dubuisson, R. Schill, M.-P. Hugon, I. Grislin and J.-L. Seran: 18 th Int. Symp., Effects of Radiation on Materials: ASTM STP 1325, ed. by R. K. Nanstad, M. L. Hamilton, F. A. Garner and A. S. Kumar, American Society for Testing and Materials, West Conshohocken, (1999), 882.
5) S. Ukai, M. Harada, H. Okada, M. Inoue, S. Nomura, S. Shikakura, K. Asabe, T. Nishida and M. Fujiwara: *J. Nucl. Mater.*, **204** (1993), 65.
6) S. Ukai, M. Harada, H. Okada, M. Inoue, S. Nomura, S. Shikakura, T. Nishida, M. Fujiwara and K. Asabe: *J. Nucl. Mater.*, **204** (1993), 74.
7) R. L. Klueh and D. R. Harries: High-Chromium Ferritic and Martensitic Steels for Nuclear Applications, ASTM Stock Number: MONO 3, (2001).
8) S. Ukai, T. Nishida and T. Yoshitake: *J. Nucl. Sci. Technol.*, **35** (1998), No. 4, 294.
9) S. Ukai, S. Mizuta, M. Fujiwara, T. Okuda and T. Kobayashi: *J. Nucl. Sci. Technol.*, **39** (2002), No.7, 778.
10) J. L. Seran, V. Levy, P. Dubuisson, D. Gilbon, A. Maillard, A. Fissolo, H. Touron, R. Cauvin, A. Chalony and E. Le. Boulbin: 15th Int. Symp., Effects of Radiation on Materials: ASTM STP 1125, ed. by R. E. Stoller, A. S. Kumar and D. S. Gelles, American Society for Testing and Materials, Philadelphia, (1992), 1209.
11) A. Uehira, S. Ukai, T. Mizuno, T. Asaga and E. Yoshida: *J. Nucl. Sci. Technol.*, **37** (2000), No. 9, 780.
12) I. Shibahara, S. Ukai, S. Onose and S. Shikakura: *J. Nucl. Mater.*, **204** (1993), 131.
13) S. Ukai, T. Okuda, M. Fujiwara, T. Kobayashi, S. Mizuta and H. Nakashima: *J. Nucl. Sci. Technol.*, **39** (2002), No. 8, 872.
14) Y. Tateishi, S. Yuhara, I. Shibahara, M. Ito, S. Nomura, Y. Sato, E. Yoshida and S. Shikakura: *J. Nucl. Sci. Technol.*, **26** (1989), No. 1, 132.
15) T. Okuda and M. Fujiwara: *J. Mater. Sci. Lett.*, **14** (1995), 1600.
16) B. Sundman: Thermo-Calc User's guide, Division of Computational Thermodynamics, Dept. Materials Science and Engineering, Royal Institute of Technology, Stockholm, Sweden, (1993).